https://doi.org/10.5194/amt-2020-353
Preprint. Discussion started: 14 September 2020

Atmospheric Measurement Techniques Discussions

Error analyses of a multistatic meteor radar system to obtain a 3-dimensional spatial resolution distribution

Wei Zhong[1], Xianghui Xue[1,2,3], Wen Yi[1,2], Iain M. Reid[4,5] Tingdi Chen[1,2,3], Xiankang Dou[1,6]

[1]CAS Key Laboratory of Geospace Environment, Department of Geophysics and Planetary Sciences, University of Science and Technology of China, Hefei, China
[2]Mengcheng National Geophysical Observatory, School of Earth and Space Sciences, University of Science and Technology of China, Heifei, China
[3]CAS Center for Excellence in Comparative Planetology, Heifei, China
[4]ATRAD Pty Ltd., Thebarton, South Australia, Australia
[5]School of Physical Sciences, University of Adelaide, Adelaide, South Australia, Australia
[6]Wuhan University, Wuhan, China

Correspondence to: Xianghui Xue (xuexh@ustc.edu.cn)

Abstract: In recent years, the concept of multistatic meteor radar systems has attracted the attention of the atmospheric radar community, focusing on the mesosphere and lower thermosphere (MLT). Recently, there have been some notable experiments using multistatic meteor radar systems (Chau et al., 2019; Spargo et al., 2019; Stober and Chau, 2015; Stober et al., 2018). Good spatial resolution is vital for meteor radars because nearly all parameter inversion processes rely on the accurate location of the meteor trail reflecting points. It is timely then for a careful discussion focussed on the error distribution of multistatic meteor radar systems. In this study, we discuss the measurement errors that affect the spatial resolution and obtain the resolution distribution in 3-dimensional space for the first time. The spatial resolution distribution can both help design a multistatic meteor radar system and improve the performance of existing radar systems. Moreover, the spatial resolution distribution allows the accuracy of retrieved parameters such as the wind field to be determined.

1 Introduction

The mesosphere and lower thermosphere (MLT) is a transition region from the neutral to the partially ionized atmosphere. It is dominated by the effects of atmospheric waves, including planetary waves, tides and gravity waves. It is also a relatively poorly sampled part of the Earth's atmosphere by ground based instruments. One widely used approach is the meteor radar technique. The ablation of incoming meteors in the MLT region, i.e., ~80 – 110 km, creates layers of metal atoms, which can be observed from the ground by photometry or lidar (Jia et al., 2016; Xue et al., 2013). During meteor ablation, the trails caused by small meteor particles provide a strong atmospheric tracer within the MLT region that can be continuously detected by meteor radar regardless of weather conditions. Consequently, the meteor radar technique has been a powerful tool for studying MLT for decades (Hocking et al., 2001; Holdsworth et al., 2004; Yi et al., 2018). Most modern meteor radars are monostatic and this has two main limitations in retrieving the complete wind field. Firstly, limited meteor rates and relatively low measurement accuracies necessitate that all measurements in the same height range be processed to calculate a "mean" wind. Secondly, traditional monostatic radars retrieve wind fields based on the assumption of a homogenous wind field in the horizontal direction and a zero wind in the vertical direction.

The latter conditions can be relaxed if the count rates are high and the detections are distributed through a representative range of azimuths. If this is the case, a version of a Velocity Azimuth Display (VAD) analysis as first applied to scanning weather radars for longer period motions can be applied by expanding the zonal and meridional winds using a truncated Taylor expansion (Browning and Wexler, 1968). This is because each valid meteor detection yields a radial velocity in a particular look direction of the radar. The radar is effectively a multi-beam Doppler radar where the "beams" are determined by the meteor detections. If there are enough suitably distributed detections in azimuth in a given observing period, the Taylor expansion approach using cartesian coordinates yields the mean zonal and meridional wind components (u_0, v_0), and the stretching $\left(\frac{\partial u}{\partial x}-\frac{\partial v}{\partial y}\right)$ and shearing $\left(\frac{\partial u}{\partial y}+\frac{\partial v}{\partial x}\right)$ deformations of the wind field from an analysis of the radial velocities. If a measure of the vertical wind is available, then the horizontal divergence $\left(\frac{\partial u}{\partial x}+\frac{\partial v}{\partial y}\right)$ can also be obtained (assuming a uniform vertical wind over the observing volume). Generally, meteor radars do not provide a reliable measure of the vertical wind component. In addition, because the radar can only retrieve the wind projection in the radial direction as measured from the radar, the vorticity $\left(\frac{\partial v}{\partial x}-\frac{\partial u}{\partial y}\right)$ of the wind field is not available. This is common to all monostatic radar systems and a discussion of measurable parameters in the context of multiple fixed beam upper atmosphere Doppler radars is given by (Reid, 1987). Even by releasing the assumption of a homogeneous wind field and using the more advanced Volume Velocity Processing (VVP) (Philippe and Corbin, 1979) to retrieve the wind field, the horizontal gradients of the wind field cannot be recovered due to the lack of vorticity information. To obtain a better understanding of the spatial variation of the MLT region wind field, larger area observations (and hence higher meteor count rates) and measurements of the non-homogenous wind field are needed. An extension of the traditional monostatic meteor technique is required to satisfy these needs.

To resolve the limitations outlined above, the concept of multistatic meteor radar systems, such as MMARA (multi-static and multi-frequency agile radar for investigations of the atmosphere) (Stober and Chau, 2015) and SIMO (single input multiple output) (Spargo et al., 2019), MIMO (multiple input multiple output radar) (Chau et al., 2019) have been designed and implemented (Stober et al., 2018). Multistatic systems can utilize the forward scatter of meteor trails, thus providing another perspective for observing the MLT. Multistatic meteor radar systems have many advantages over traditional monostatic meteor radars, such as obtaining higher-order wind field information and covering wider observation areas. There have been some particularly innovative studies using multistatic meteor radar systems in recent years. For example, by combining MMARA and the continuous wave multistatic radar technique (Vierinen et al., 2016), Stober and Chau et al. built a 5-station total 7-link multistatic radar network covering an approximately 600 km×600 km region in Germany to retrieve an arbitrary non-homogenous wind field with a 30 km×30 km horizontal resolution (Stober et al., 2018). Stober et al. used two adjacent traditional monostatic specular meteor radars in northern Norway to obtain horizontal divergence and vorticity (Chau et al., 2017). Other approaches, such as the novel multistatic meteor radar data processing method (Vierinen et al., 2019) and the compressed sense method in MIMO sparse signal recovery (Urco et al., 2019), are described in the references in these papers. Analysing spatial resolution in regions of interest is a fundamental but difficult topic for meteor radar systems. Meteor radar systems transmit radio waves and then receive radio waves using a cluster of receiver antennas; commonly five antennas as in the Jones et al. configuration (Jones et al., 1998). By analysing the cross correlation of received signals, we can determine the angle of arrival (AoA), that is, the zenith angle θ and azimuth angle ϕ. By measuring the wave propagation time, we can obtain the range. Most meteor radar systems rely on specular reflections from meteor trails. Thus, by combining the AoA and the range information and then using geometric analysis, we can determine the location of meteor trails. Accurately locating meteor trail reflection points is important since atmospheric parameter retrieval (such as the wind field or the temperature) depends on the location information of meteor trails. The location accuracy, namely, the spatial resolution, determines the reliability of the retrieved parameters. For multistatic meteor radar systems that can relax the assumption of a homogenous horizontal wind field, the resolution distribution becomes a more important issue because the horizontal spatial resolution affects the accuracy of the retrieved horizontal wind field gradient.

There are a number of studies that discuss AoA measuring errors (Kang, 2008; Vaudrin et al., 2018; Younger and Reid, 2017). However, those error analyses emphasize the receiving antennas and seldom discuss the influence of a multistatic configuration on the spatial resolutions. Moreover, those analyses consider the error propagation starting from the original signals received by the cluster of antennas; therefore, the results of AoA errors become too intricate to utilize in further resolution analyses. Hocking developed a vertical resolution analysis model in a 2-dimensional baseline vertical plane (Hocking, 2018), which simplifies the error propagation process in receiver antennas to emphasize the bistatic configuration. However, Hocking's model (HM hereafter) has nothing to do with the distance between the transmitter and the receiver which will be explained in this paper. Moreover, for practical purposes, the 3-dimensional spatial distribution of both horizontal resolution and vertical resolution should be considered.

Although multistatic meteor radar systems have developed well experimentally in recent years, the reliability of retrieved atmospheric parameters lacks discussion. To better understand the reliability of the obtained atmospheric parameters, quantitative error analyses are necessary. In this paper, we analyse the multistatic meteor radar resolution distribution in a three-dimensional space for both vertical and horizontal resolutions for the first time. This work allows for the analysis of the reliability of retrieved atmospheric parameters.

2 Analytical Method

In the HM, measuring errors that affect vertical resolution can be classified into two types (Hocking, 2018) : those caused by the zenith angle measuring error $\delta\theta$ and those caused by the pulse-length effect on vertical resolution. In the HM, the receiver is reduced to a simple antenna pair that is collinear to the baseline (see figure 1) by considering only a two-dimensional vertical plane. The antenna pair in the HM is equal to one antenna pair in the Jones configuration, which is comprised of three collinear

https://doi.org/10.5194/amt-2020-353
Preprint. Discussion started: 14 September 2020

Atmospheric Measurement Techniques Discussions

antennas and is usually in a $2\lambda\backslash 2.5\lambda$ configuration. The radio wave phase difference between antenna pairs is denoted as $\Delta\Psi$. In meteor radar systems, there are acceptable phase difference measuring errors $\delta(\Delta\Psi)$. A higher value of $\delta(\Delta\Psi)$ means that more signals will be judged as meteor trails and that there will be more misidentifications as well. $\delta(\Delta\Psi)$ is usually set to approximately 30° (Hocking, 2018; Younger and Reid, 2017) in meteor radar systems. In the HM, the AoA error $\delta\theta$ is due to $\delta(\Delta\Psi)$, which is a constant. Therefore, the error propagation in the receiver is very simple, and $\delta\theta$ is inversely proportional to the cosine of the zenith.

Our model considers a multistatic system with multiple transmitters and one receiving array in 3-dimensional space (figure 2). The receiving array is in the Jones configuration, which in a plan view layout can be “cross-shaped”, “T-shaped” or “L-shaped”. The five receive antennas should be in the same horizontal plane and constitute two orthogonal antenna arms. To avoid a complex AoA error analyses and to place emphasis on multistatic configurations, we treat the two receiver phase difference measuring errors ($\delta(\Delta\Psi_1)$ and $\delta(\Delta\Psi_1)$) in the two orthogonal antenna arrays as constants. Therefore, the AoA measuring errors (including zenith and azimuth angle measuring errors $\delta\theta$, $\delta\phi$) can simply be a function of zenith and azimuth angle. The distance between the meteor trail reflection points and the receiver is denoted as R_t. R_t can be determined by combining the AoA, baseline length d, and radio wave propagating distance R (Stober and Chau, 2015) as:

$$R_t = \frac{R^2 - d^2}{2(R - d\cos\alpha)} \qquad (1)$$

where α is the angle between the baseline (axis-X_i') and the line from the receiver to the meteor trail reflection point. In eq. (1), the multistatic configuration will influence the accuracy of R_t (denoted as δR_t). In our model, we consider the error term δR_t which is ignored in the HM. δR_t is a function of the AoA measuring errors ($\delta\theta$ and $\delta\phi$) and the wave propagation distance measuring error (denoted as δR). δR is caused by the measuring error of the wave propagation time δt, which is approximately $21\mu s$ (Kang, 2008). Thus, δR can be set as a constant and $\delta R = c\,\delta t = 6.3km$. It is worth noting that the maximum unambiguous range for pulse meteor radars is determined by the pulse repetition frequency (PRF) (Hocking et al., 2001; Holdsworth et al., 2004). In our model, for the region where R is more than c/PRF (where c is the speed of light), δR is set to positive infinity.

To better depict the multistatic system configuration, we need to establish appropriate coordinate systems (figure 3). The spatial configuration of the receiver horizontal plane is determined by the local topography and the antenna configuration. We establish a left-hand coordinate system XYZ to depict the receiver horizontal plane. XYZ is fixed on the receiver and thus will rotate with the 5-antenna horizontal plane. The coordinate origin of XYZ is on the receiver. Axis-Z is collinear with the antenna boresight and perpendicular to the horizontal plane. Axis-X and axis-Y are in the horizontal plane and collinear with the arms of the two orthogonal antenna arrays. Therefore, the zenith angle and azimuth angle are conveniently represented in the XYZ coordinate system. For different transmitters T_i, the baseline direction and distance between T_i and the receiver are different. It is convenient to analyse the range information in the plane that goes through the baseline and meteor trail reflection points (figure 4). Thus, we establish a class of coordinate systems $X_i^{'}\,Y_i^{'}\,Z_i^{'}$ for each T_i. The coordinate origins of $X_i^{'}\,Y_i^{'}\,Z_i^{'}$ are

https://doi.org/10.5194/amt-2020-353
Preprint. Discussion started: 14 September 2020

Atmospheric Measurement Techniques Discussions

all on the receiver. We stipulate that axis-$X_i^{'}$ points to transmitter $\boldsymbol{i}$ ($\mathrm{T_i}$). Axis-$Y_i^{'}$ and axis-$Z_i^{\prime}$ need to satisfy the right-hand corkscrew rule with axis-$X_i^{'}$. Each transmitter, T_i, and the receiver constitute a radar link, which is referred to as L_i. We will deal with the range information for each L_i in $X_i^{'}\ Y_i^{'}\ Z_i^{'}$. Spatial resolution distributions for every L_i need to be compared in the same coordinate system, and this coordinate system needs to be convenient for retrieving wind fields. Therefore, we establish a local WNU (west-north-up) coordinate system $X_0^{'}\ Y_0^{'}\ Z_0^{\prime}$ on the receiver. The origin of $X_0^{'}\ Y_0^{'}\ Z_0^{'}$ is on the receiver with axis-X pointing to the west, axis-Y to the north, and axis-Z pointing up. All spatial resolution distributions for each L_i will ultimately be converted to $X_0^{'}\ Y_0^{'}\ Z_0^{\prime}$.

We specify that clockwise rotation is in the right-hand corkscrew rule. By rotating clockwise in order of $\psi_x^{\mathrm{X,i}}$, $\psi_y^{Y,\mathrm{i}}$ and $\psi_z^{Z,\mathrm{i}}$ about axis-X, Y and Z, respectively, we can transform XYZ to $\mathrm{X_i^{'}\ Y_i^{'}\ Z_i^{'}}$. It is worth mentioning that $X_i^{'}\ Y_i^{'}\ Z_i^{'}$ is non-unique because any rotation about axis-$X_i^{'}$ can obtain one $X_i^{'}\ Y_i^{'}\ Z_i^{'}$. Hence, $\psi_x^{\mathrm{X,1}}$ can be set to any values. Similarly, by rotating clockwise in order of $\psi_x^{\mathrm{i,0}}$, $\psi_y^{i,0}$ and $\psi_z^{i,0}$ about axis-X, Y and Z, respectively, we can transform $X_i^{'}\ Y_i^{'}\ Z_i^{'}$ to $X_0^{'}\ Y_0^{'}\ Z_0^{'}$. To realize the coordinate transformation between those three coordinate systems, we now introduce coordinate rotation matrix $A_R(\psi_x, \psi_y, \psi_z)$. Using A_R, we can transform the coordinate point or vector presentation from one system to another. The details of the coordinate rotation matrix $A_R(\psi_x, \psi_y, \psi_z)$ can be seen in **Appendix (A.1)**.

The analytical method of the spatial resolution of each radar link is the same. The difference between those radar links is only the value of the six coordinates rotation angle ($\psi_x^{\mathrm{X,i}}$, $\psi_y^{Y,\mathrm{i}}$ and $\psi_z^{Z,\mathrm{i}}$; $\psi_x^{\mathrm{i,0}}$, $\psi_y^{i,0}$ and $\psi_z^{i,0}$) and baseline distance **d**. In the following, we analyse the spatial resolution of one radar link, L_i as an example. The measurement errors, which affect the spatial resolution, cause a location bias in the specular reflection point. These errors can be classified into two types: E_1 is caused by measurement errors in the receiver, and E_2 is due to the pulse length. These two errors are mutually independent. Hence, the total error (E_{total}) in the form of the mean square error (MSE) can be expressed as:

$$\mathrm{E_{total}^2 = E_1^2 + E_2^2} \tag{2}$$

E_1 is related to three indirect measuring errors, $\delta\theta$, $\delta\phi$ and δR_t, which are zenith, azimuth and radial distance measuring errors, respectively. In XYZ, E_1 can be decomposed into three orthogonal error vectors using $\delta\theta$, $\delta\phi$ and δR_t (figure 4(c)) $\delta\theta$ and $\delta\phi$ are the functions of phase difference measuring errors $\delta(\Delta\Psi_1)$ and $\delta(\Delta\Psi_2)$. $\Delta\Psi_1$ and $\Delta\Psi_2$ are the two orthogonal antenna arrays' phase differences. Those phase differences measuring errors $\delta(\Delta\Psi_1)$ and $\delta(\Delta\Psi_2)$ are treated as two independent measuring errors. Through derivation, the true error of $\delta\theta$ and $\delta\phi$ can be expressed as:

$$\delta\theta = \frac{\lambda}{2\pi D_1}\frac{\cos\phi}{\cos\theta}\delta(\Delta\Psi_1) + \frac{\lambda}{2\pi D_2}\frac{\sin\phi}{\cos\theta}\delta(\Delta\Psi_2) \tag{3}$$

$$\delta\phi = \frac{\lambda}{2\pi D_2}\frac{\cos\phi}{\sin\theta}\delta(\Delta\Psi_2) - \frac{\lambda}{2\pi D_1}\frac{\sin\phi}{\sin\theta}\delta(\Delta\Psi_1) \tag{4}$$

https://doi.org/10.5194/amt-2020-353
Preprint. Discussion started: 14 September 2020

where λ is the wavelength used in the radar system. θ and ϕ are the zenith angle and azimuth angle, respectively. The details can be seen in **Appendix (A.2).** It is worth noting that $\delta\theta$ and $\delta\phi$ are not independent. The expectation value $E(\delta\theta \cdot \delta\phi)$ is not identical to zero unless $\frac{E\left(\delta^2(\Delta\Psi_1)\right)}{D_1^2}$ equals.$\frac{E\left(\delta^2(\Delta\Psi_2)\right)}{D_2^2}$. The true error of δR_t can be expressed as a function of δR, $\delta\theta$ and $\delta\phi$ as:

$$\delta R_t = F(\delta R\,, \delta\theta\,, \delta\phi) = f_R(\theta,\phi)\delta R + f_\theta(\theta,\phi)\delta\theta + f_\phi(\theta,\phi) \tag{5}$$

$f_R(\theta,\phi)$, $f_\theta(\theta,\phi)$ and $f_\phi(\theta,\phi)$ are the weight functions of δR_t. δR is the wave propagating distance measuring error. The details about the weight function and deduction can be found in **Appendix(A.3)**. Obviously, δR_t is related to the geometry of the multistatic meteor radar system. Thus far, the true error vectors of E_1 can be decomposed into three orthogonal vectors in coordinate XYZ, which are $\overrightarrow{\delta R_t}$, $\overrightarrow{R_t\delta\theta}$ and $\overrightarrow{R_t sin\theta\delta\phi}$ (figure 4(c)). These three vectors can be expressed in XYZ as:

$$\overrightarrow{\delta R_t} = \delta R_t(\sin\theta\cos\phi, \sin\theta\sin\phi, \cos\theta)^T \tag{6}$$

$$\overrightarrow{R_t\delta\theta} = R_t\delta\theta(-\cos\theta\cos\phi, -\cos\theta\sin\phi, \sin\theta)^T \tag{7}$$

$$\overrightarrow{R_t sin\theta\delta\phi} = R_t\sin\theta\delta\phi(-\sin\phi, \cos\phi, 0)^T \tag{8}$$

E_2 is related to the geometry of the radio propagating path and works only in pulse radar systems. The pulse might be reflected anywhere within the pulse length (figure 4(b)). Hence, there exists an unclear area, and we denote it as error vector $\overrightarrow{DA}$, where D is the median point of isosceles triangle ΔABC's side BC. From the geometric relationship, the error vector $\overrightarrow{DA}$ in $X_0^{'}\,Y_0^{'}\,Z_0^{'}$ is:

$$\overrightarrow{DA}= \left(\frac{(2-a_1-a_2)x_0+d(a_1-1)}{2}\,, \frac{2-a_1-a_2}{2}\mathbf{y_0}\,, \frac{2-a_1-a_2}{2}\mathbf{z_0}\right)^T \tag{9}$$

S is half pulse length and $a_1 = \frac{R_t-S}{R_t}$. $a_2 = \frac{R_1-S}{R_1}$. **d** is the straight-line distance between the receiver and T_i (baseline length). Here, we introduced two types of errors in different coordinate systems, and we now need to transform them into local coordinates $X_0^{'}\,Y_0^{'}\,Z_0{}'$, which is convenient for analysing wind fields. The true error vectors $\overrightarrow{\delta R_t}$, $\overrightarrow{R_t\delta\theta}$ and $\overrightarrow{R_t sin\theta\delta\phi}$ need two coordinate transformations, that is, from XYZ to $X_i^{'}\,Y_i^{'}\,Z_i^{'}$ and then to $X_0^{'}\,Y_0^{'}\,Z_0^{'}$. By deducing, the true error of E_1 can be expressed as vector $\left(\delta_{(1)}X_0^{'}\,, \delta_{(1)}Y_0^{'}\,, \delta_{(1)}Z_0^{'}\right)^T$ in $X_0^{'}\,Y_0^{'}\,Z_0'$:

$$\begin{pmatrix}\delta_{(1)}X'_0\\ \delta_{(1)}Y'_0\\ \delta_{(1)}Z'_0\end{pmatrix} = \begin{pmatrix}X'_0(\delta R_t) & X'_0(\delta\theta) & X'_0(\delta\phi)\\ Y'_0(\delta R_t) & Y'_0(\delta\theta) & Y'_0(\delta\phi)\\ Z'_0(\delta R_t) & Z'_0(\delta\theta) & Z'_0(\delta\phi)\end{pmatrix}\cdot\begin{pmatrix}f_R(\theta,\phi) & f_\theta(\theta,\phi) & f_\phi(\theta,\phi)\\ 0 & R_t & 0\\ 0 & 0 & R_t\sin\theta\end{pmatrix}\cdot\begin{pmatrix}\delta R\\ \delta\theta\\ \delta\phi\end{pmatrix} \tag{10}$$

We denote the first term in the right formula as the error projection matrix, which transforms $\overrightarrow{\delta R_t}$, $\overrightarrow{R_t\delta\theta}$ and $\overrightarrow{R_t sin\theta\delta\phi}$ in XYZ to axis $X_0^{'}, Y_0^{'}$ *and* Z_0'. The second matrix term is referred to as the error weight matrix, which can assemble $\delta R, \delta\theta$

https://doi.org/10.5194/amt-2020-353
Preprint. Discussion started: 14 September 2020

and $\delta\phi$ to $\overrightarrow{\delta R_t}$, $\overrightarrow{R_t\delta\theta}$ and $\overrightarrow{R_t sin\theta\delta\phi}$. The matrix details can be seen in **Appendix (A.5)**. However, $\delta\theta$ and $\delta\phi$ are not independent. To calculate the mean square error (MSE), we need to transform $\delta\theta$ and $\delta\phi$ into two independent errors: $\delta(\Delta\Psi_1)$ and $\delta(\Delta\Psi_2)$. Using eq. (3) and (4), we can transform vector $(\delta R\ ,\ \delta\theta\ ,\ \delta\phi)^T$ to three independent measuring errors
185 δR, $\delta(\Delta\Psi_1)$ and $\delta(\Delta\Psi_2)$ as:

$$\begin{pmatrix}\delta R\\ \delta\theta\\ \delta\phi\end{pmatrix} = \begin{pmatrix} 1 & 0 & 0 \\ 0 & \frac{\frac{\lambda}{2\pi}}{cos\theta}\frac{cos\phi}{D_1} & \frac{\frac{\lambda}{2\pi}}{cos\theta}\frac{sin\phi}{D_2} \\ 0 & -\frac{\frac{\lambda}{2\pi}sin\phi}{sin\theta D_1} & \frac{\frac{\lambda}{2\pi}cos\phi}{sin\theta D_2}\end{pmatrix}\begin{pmatrix}\delta R\\ \delta(\Delta\Psi_1)\\ \delta(\Delta\Psi_2)\end{pmatrix} \tag{11}$$

We denote the first term on the right as the base transformation matrix. We denote the dot product of the error projection matrix, error weight matrix and base transformation matrix as W_{EP}. We refer to W_{EP} as the error propagation matrix. W_{EP} is a 3×3 matrix, and we denote the element in it as W_{ij}. Then, we define $SW_{EP} = W_{ij}^2$. Thus, E_1 in the form of MSE square
190 can be expressed as vector $(\delta^2_{(1)}X_0^{'}\ ,\ \delta^2_{(1)}Y_0'\ ,\ \delta^2_{(1)}Z_0^{'}\ )^T$ in $X_0^{'}\ Y_0^{'}\ Z_0^{'}$:

$$\begin{pmatrix}\delta^2_{(1)}X_0^{'}\\ \delta^2_{(1)}Y_0^{'}\\ \delta^2_{(1)}Z^{'}{}_0\end{pmatrix} = SW_{EP}\begin{pmatrix}\delta^2 R\\ \delta^2(\Delta\Psi_1)\\ \delta^2(\Delta\Psi_2)\end{pmatrix} \tag{12}$$

For E_2, true error vector $\overrightarrow{DA}$ needs transformation from $X_i^{'}\ Y_i^{'}\ Z_i^{'}$ to $X_0^{'}\ Y_0^{'}\ Z_0^{'}$. Therefore, the true error of E_2 can be expressed as vector $X_0^{'}\ Y_0^{'}\ Z_0^{'}$:

$$\begin{pmatrix}\delta_{(2)}X_0^{'}\\ \delta_{(2)}Y_0^{'}\\ \delta_{(2)}Z'_0\end{pmatrix} = A_R(\Psi_x^{i,0},\Psi_y^{i,0},\Psi_z^{i,0})\cdot\overrightarrow{\mathrm{DA}} \tag{13}$$

195 From eq. (2), the MSE of E_{total} squared for radar link L_i can be expressed as vector $(\delta_{total}X_0^{'}\ ,\ \delta_{total}Y_0^{'}\ ,\ \delta_{total}Z_0^{'}\ )^T$ in $X_0^{'}\ Y_0^{'}\ Z_0^{'}$:

$$\begin{pmatrix}\delta^2_{total}X_0^{'}\\ \delta^2_{total}Y_0^{'}\\ \delta^2_{total}Z^{'}{}_0\end{pmatrix} = \begin{pmatrix}\delta^2_{(1)}X_0^{'}\\ \delta^2_{(1)}Y_0^{'}\\ \delta^2_{(1)}Z^{'}{}_0\end{pmatrix} + \begin{pmatrix}\delta^2_{(2)}X_0^{'}\\ \delta^2_{(2)}Y_0^{'}\\ \delta^2_{(2)}Z'_0\end{pmatrix} \tag{14}$$

3 Results and Discussion

We wrote a program to study the method above. The code is written in the python language and is president in supplement.
200 To calculate a special configuration of a multistatic radar system, we initially set six coordinate transformation angles ($\psi_x^{X,i}$,

https://doi.org/10.5194/amt-2020-353
Preprint. Discussion started: 14 September 2020

Atmospheric Measurement Techniques Discussions

$\psi_y^{Y,\mathrm{i}}$ and $\psi_z^{Z,\mathrm{i}}$; $\psi_x^{\mathrm{i},0}$, $\psi_y^{i,0}$ and $\psi_z^{i,0}$) and baseline length (straight-line distance **d**) for each radar link L_i. For a given setting of radar link $\mathrm{L_i}$, the program will output data in the form of MSE square (E_{total}^2: $\delta_{total}^2 X_0^{'}$, $\delta_{total}^2 Y_0^{'}$, $\delta_{total}^2 Z_0^{'}$; E_1^2: $\delta_{(1)}^2 X_0^{'}$, $\delta_{(1)}^2 Y_0^{'}$, $\delta_{(1)}^2 Z_0^{'}$; E_2^2: $\delta_{(2)}^2 X_0^{'}$, $\delta_{(2)}^2 Y_0'$, $\delta_{(2)}^2 Z_0^{'}$). The MSE of these errors can be positive or negative and the spatial resolutions are twice the absolute of MSE.

The HM analyses vertical resolution (corresponding to $\delta Z_0'$ in our paper) only in a 2-dimensional vertical plane (corresponding to the $X_0^{'}\ Z_0^{'}$ plane in our paper). To compare with Hocking's work, we set all six coordinate transformation angles to zero and **d** to 300 km. The half pulse length is set to 2 km and $\delta(\Delta\Psi_1)$ to 35°. Setting $\delta(\Delta\Psi_2)$ to zero and calculating in only the $X_0^{'}\ Z_0^{'}$ plane should degrade our model into Hocking's 2-dimensional analysis model. However, the settings above do not make perfect sense because Hocking's model ignores δR_t. In fact, Hocking's model considers only E_2 and $\overrightarrow{R_t\delta\theta}$ in the $X_0^{'}\ Z_0^{'}$ plane. Hence, we need to further set $f_R(\theta,\phi)$, $f_\theta(\theta,\phi)$ and $f_\phi(\theta,\phi)$ to zero. Thus, our model totally degrades into Hocking's model. Note that our program output data is in the form of MSE squared, while Hocking's results are shown in the absolute value of MSE normalized relative to half pulse width $S/2$, which is a quarter of the resolution. Our output data go through the same process as in Hocking's work, and the result is shown in figure 5(a). Our results are the same as those in Hocking's work (Hocking, 2018). The distributions of the error terms $\overrightarrow{R_t\delta\theta}$ and E_2 are shown in the second and third subplots in figure 5(a) from left to right, respectively. In most cases, E_2 is an order of magnitude smaller than $\overrightarrow{R_t\delta\theta}$. Only in the region directly above the receiver does E_2 have the same magnitude as $\overrightarrow{R_t\delta\theta}$. In other words, only in the region directly above the receiver can E_2 influence the total resolution. $\mathrm{E_2}$ is related to the bistatic configuration, but $\overrightarrow{R_t\delta\theta}$ is not. Therefore, in the HM, the distribution of the total resolution is nearly unchanged with varying d (figure 5(b) and 5(c)). After adding the error term $\overrightarrow{\delta R_t}$, which is related to the bistatic configuration, the normalized vertical spatial resolution distribution is shown in figure 6. The vertical spatial resolution in most vertical planes surpasses 4 km (corresponding to 1 km in normalized spatial resolution). With increasing **d**, the resolution distribution is holistically compressed and is opposite to the transmitter.

Now, we analyse spatial resolutions in 3-dimensional space in our model. We set $\delta(\Delta\Psi_2)$ and D_2 the same as $\delta(\Delta\Psi_1)$ and D_1 ($\delta(\Delta\Psi_1)=\delta(\Delta\Psi_2)=35^\circ$,$\frac{D_1}{\lambda}=\frac{D_2}{\lambda}=4.5$). Taking normalized spatial resolution distributions in the $X_0^{'}\ Y_0'$ plane at 90 km as an example, see figure 7, the baseline length is 300 km, and the angle between the baseline and $X_0^{'}$ is 45°. Other parameter settings can be seen in Table 1. In the horizontal plane, $\mathrm{E_1}$ is an order of magnitude larger than $\mathrm{E_2}$ in the $X_0^{'}$,$Y_0^{'}$,Z_0' direction in most regions. Therefore, the total spatial resolution in the $X_0^{'}$,$Y_0^{'}$,$Z_0^{'}$ direction is mainly controlled by $\mathrm{E_1}$. The horizontal spatial resolutions distributions will split into two parts in a relatively long baseline length due to the error term "$\overrightarrow{\delta R_t}$". Because we observe the errors in $X_0^{'}\ Y_0^{'}\ Z_0'$, the horizontal resolution distributions are not symmetric about the baseline. The area of vertical spatial resolution less than 12 km (corresponding to 3 km in normalized spatial resolution) is much smaller than the area of horizontal resolution less than 12 km. The vertical resolution distribution becomes compressed

https://doi.org/10.5194/amt-2020-353
Preprint. Discussion started: 14 September 2020

Atmospheric Measurement Techniques Discussions

and tends to move opposite to the transmitter. This tendency can also be seen from the perspective of the vertical plane (figure 6).

Figure 8 shows the normalized spatial resolution distributions in other parameter settings. The parameter setting details are shown in Table 1. Traditional monostatic meteor radar is a special case of a multistatic meteor radar system whose baseline length is zero. Figure 8(a) shows the normalized spatial resolution distributions of monostatic meteor radar. The spatial resolution distributions are highly symmetrical and correspond to the real characteristics of monostatic meteor radar. Comparing figure 8(b) and figure 8(c), the slight tilting of the receiver horizontal plane ($\psi_x^{X,i}$=$\psi_y^{Y,i} = 5°$) will cause horizontal spatial distributions to apparently change. In practical applications, the Earth's curvature, local topography or receiver horizontal plane calibration error all lead to the receiver horizontal plane tilting. Thus, this kind of slant should also be taken into account for multistatic meteor radar systems.

As mentioned above, the AoA error analysis can be complex. Hence, we have greatly simplified the error propagation process to emphasize the multistatic configuration. If analysing AoA errors starts from the original voltage signals, the error propagation process will change with the specific receiver interferometer configuration and specific signal processing method. In practical situations for an unusual receiver antenna configuration or new original signal processing algorithm, we can establish an error propagation process based on specific circumstances. The distribution of $\delta\theta$ and $\delta\phi$ can be obtained using the established error propagation process. Substituting $\delta(\Delta\Psi_1)$ and $\delta(\Delta\Psi_2)$ into other mutually independent direct measuring errors in a practical situation, and then establishing a new base transformation matrix in eq. (11) using the error propagation analysis above, we can obtain a new eq. (11). Substituting eq. (11) into the new eq. (11), our model will still work.

4 Conclusion

In this study, we presented the preliminary results of our error analysis model. Our model can calculate the resolutions in the X_0', Y_0', Z_0' direction for an arbitrary configuration in three-dimensional space. The true location of a detected meteor trail reflection point can be in equal probability distributed within the spatial resolution region around the measured location. Higher values of spatial resolution mean that this region needs more meteor counts or averaging to obtain a reliable accuracy. Our model shows that the spatial configuration of a multistatic system will greatly influence the resolution distribution in local coordinates $X_0'Y_0'Z_0'$ and thus will in turn influence the retrieval accuracy of atmospheric parameters such as wind fields. The multistatic meteor radar system's spatial resolution analysis is a key point in analysing the accuracy of retrieved wind and other parameters. We will calculate retrieval error analyses on real data in future work. Multistatic radar systems come in many types, and our work in this paper considers only single-input (single-antenna transmitter in each T_i) and multi-output (5-antenna interferometric receiver) pulse radar systems. Although single-input multi-output (SIMO) pulse meteor radar is a classic meteor radar system, other meteor radar systems, such as continuous wave radar systems and MISO (multiple-antenna transmitter and single-antenna receiver), show good experimental results and have some advantages over SIMO systems. Using different types of meteor radar systems to constitute the meteor radar network is the future trend and we will add the spatial

https://doi.org/10.5194/amt-2020-353
Preprint. Discussion started: 14 September 2020

resolution analyses of other system to the frame of our model in this paper. We will validate and apply the error analyses of spatial resolution in horizontal wind determination in a multistatic meteor radar system, which will be built soon in China.

Code availability. The program to calculate the 3D spatial resolution distributions are available in supplement.

Author contributions：W.Z, X.X, W.Y designed the study. W.Z deduced the formulas and wrote the program. W.Z wrote the paper for the first version. I.R supervised the work and provided valuable comments. I.R revised the paper. All of the authors discussed the results and commented on the paper.

Competing interest. The authors declare no conflicts of interests

Acknowledgements. This work is supported by the National Natural Science Foundation of China (41774158, 41974174, 41831071 and 41904135), the B-type Strategic Priority Program of CAS Grant No. XDB41000000, the CNSA pre-research Project on Civil Aerospace Technologies No. D020105, the Fundamental Research Funds for the Central Universities, and the Open Research Project of Large Research Infrastructures of CAS “Study on the interaction between low/mid-latitude atmosphere and ionosphere based on the Chinese Meridian Project.”

Reference

Browning, K. A., and Wexler, R.: The Determination of Kinematic Properties of a Wind Field Using Doppler Radar, Journal of Applied Meteorology, 7, 105-113, 10.1175/1520-0450(1968)007<0105:Tdokpo>2.0.Co;2, 1968.

Chau, J. L., Stober, G., Hall, C. M., Tsutsumi, M., Laskar, F. I., and Hoffmann, P.: Polar mesospheric horizontal divergence and relative vorticity measurements using multiple specular meteor radars, Radio Science, 52, 811-828, 10.1002/2016rs006225, 2017.

Chau, J. L., Urco, J. M., Vierinen, J. P., Volz, R. A., Clahsen, M., Pfeffer, N., and Trautner, J.: Novel specular meteor radar systems using coherent MIMO techniques to study the mesosphere and lower thermosphere, Atmos. Meas. Tech., 12, 2113-2127, 10.5194/amt-12-2113-2019, 2019.

Hocking, W. K., Fuller, B., and Vandepeer, B.: Real-time determination of meteor-related parameters utilizing modem digital technology, Journal of Atmospheric and Solar-Terrestrial Physics, 63, 155-169, 10.1016/s1364-6826(00)00138-3, 2001.

Hocking, W. K.: Spatial distribution of errors associated with multistatic meteor radar, Earth, Planets and Space, 70, 93, 10.1186/s40623-018-0860-2, 2018.

Holdsworth, D. A., Reid, I. M., and Cervera, M. A.: Buckland Park all-sky interferometric meteor radar, Radio Science, 39, 10.1029/2003rs003014, 2004.

Jia, M. J., Xue, X. H., Dou, X. K., Tang, Y. H., Yu, C., Wu, J. F., Xu, J. Y., Yang, G. T., Ning, B. Q., and Hoffmann, L.: A case study of A mesoscale gravity wave in the MLT region using simultaneous multi-instruments in Beijing, Journal of Atmospheric and Solar-Terrestrial Physics, 140, 1-9, 10.1016/j.jastp.2016.01.007, 2016.

Jones, J., Webster, A. R., and Hocking, W. K.: An improved interferometer design for use with meteor radars, Radio Science, 33, 55-65, 10.1029/97rs03050, 1998.

Kang, C.: Meteor radar signal processing and error analysis, 2008.

Philippe, W., and Corbin, H.: On the Analysis of Single-Doppler Radar Data, Journal of Applied Meteorology - J APPL METEOROL, 18, 532-542, 10.1175/1520-0450(1979)018<0532:OTAOSD>2.0.CO;2, 1979.

Reid, I. M.: SOME ASPECTS OF DOPPLER RADAR MEASUREMENTS OF THE MEAN AND FLUCTUATING COMPONENTS OF THE WIND-FIELD IN THE UPPER MIDDLE ATMOSPHERE, Journal of Atmospheric and Terrestrial Physics, 49, 467-484, 10.1016/0021-9169(87)90041-9, 1987.

Spargo, A. J., Reid, I. M., and MacKinnon, A. D.: Multistatic meteor radar observations of gravity-wave–tidal interaction over southern Australia, Atmos. Meas. Tech., 12, 4791-4812, 10.5194/amt-12-4791-2019, 2019.

Stober, G., and Chau, J. L.: A multistatic and multifrequency novel approach for specular meteor radars to improve wind measurements in the MLT region, Radio Science, 50, 431-442, 10.1002/2014rs005591, 2015.

Stober, G., Chau, J. L., Vierinen, J., Jacobi, C., and Wilhelm, S.: Retrieving horizontally resolved wind fields using multi-static meteor radar observations, Atmos. Meas. Tech., 11, 4891-4907, 10.5194/amt-11-4891-2018, 2018.

Urco, J. M., Chau, J. L., Weber, T., Vierinen, J. P., and Volz, R.: Sparse Signal Recovery in MIMO Specular Meteor Radars With Waveform Diversity, Ieee Transactions on Geoscience and Remote Sensing, 57, 10088-10098, 10.1109/tgrs.2019.2931375, 2019.

Vaudrin, C. V., Palo, S. E., and Chau, J. L.: Complex Plane Specular Meteor Radar Interferometry, Radio Science, 53, 112-128, 10.1002/2017rs006317, 2018.

Vierinen, J., Chau, J. L., Pfeffer, N., Clahsen, M., and Stober, G.: Coded continuous wave meteor radar, Atmospheric Measurement Techniques, 9, 829-839, 10.5194/amt-9-829-2016, 2016.

Vierinen, J., Chau, J. L., Charuvil, H., Urco, J. M., Clahsen, M., Avsarkisov, V., Marino, R., and Volz, R.: Observing Mesospheric Turbulence With Specular Meteor Radars: A Novel Method for Estimating Second-Order Statistics of Wind Velocity, Earth and Space Science, 6, 1171-1195, 10.1029/2019ea000570, 2019.

Xue, X. H., Dou, X. K., Lei, J., Chen, J. S., Ding, Z. H., Li, T., Gao, Q., Tang, W. W., Cheng, X. W., and Wei, K.: Lower thermospheric-enhanced sodium layers observed at low latitude and possible formation: Case studies, Journal of Geophysical Research-Space Physics, 118, 2409-2418, 10.1002/jgra.50200, 2013.

Yi, W., Xue, X. H., Reid, I. M., Younger, J. P., Chen, J. S., Chen, T. D., and Li, N.: Estimation of Mesospheric Densities at Low Latitudes Using the Kunming Meteor Radar Together With SABER Temperatures, Journal of Geophysical Research-Space Physics, 123, 3183-3195, 10.1002/2017ja025059, 2018.

https://doi.org/10.5194/amt-2020-353
Preprint. Discussion started: 14 September 2020

Younger, J. P., and Reid, I. M.: Interferometer angle-of-arrival determination using precalculated phases, Radio Science, 52, 1058-1066, 10.1002/2017rs006284, 2017.

Appendix

A.1 Coordinates rotation matrix

For a left-handed rectangular coordinate system XYZ, we rotate clockwise Ψ_x about axis-x to obtain a new coordinate Z'. We specify that clockwise rotation is in the right-hand screw rule. A vector in XYZ, denoted as $(x, y, z)^T$, is represented as $(x', y', z')^T$ in Z'. The relationship between $(x, y, z)^T$ and $(x', y', z')^T$ is:

$$\begin{pmatrix} x' \\ y' \\ z' \end{pmatrix} = A_x(\psi_x)\begin{pmatrix} x \\ y \\ z \end{pmatrix} = \begin{pmatrix} 1 & 0 & 0 \\ 0 & cos\psi_x & -sin\psi_x \\ 0 & sin\psi_x & cos\psi_x \end{pmatrix}\begin{pmatrix} x \\ y \\ z \end{pmatrix} \tag{A1.1}$$

Similarly, we rotate clockwise Ψ_y is about axis-y to obtain a new coordinate. The presentation for a vector in new coordinates and origins can be linked by a matrix, $A_y(\psi_y)$:

$$A_y(\psi_y) = \begin{pmatrix} \cos\psi_y & 0 & \sin\psi_y \\ 0 & 1 & 0 \\ -\sin\psi_y & 0 & \cos\psi_y \end{pmatrix} \tag{A1.2}$$

we rotate clockwise Ψ_z about axis-z to obtain a new coordinate. The presentation for a vector in new coordinates and origins can be linked by a matrix, $A_z(\psi_z)$:

$$A_z(\psi_z) = \begin{pmatrix} cos\psi_z & -sin\psi_z & 0 \\ sin\psi_z & cos\psi_z & 0 \\ 0 & 0 & 1 \end{pmatrix} \tag{A1.3}$$

For any two coordinate systems, XYZ and $X'Y'Z'$, we can always rotate clockwise Ψ_x, Ψ_y and ψ_z in order of axis-X,Y,Z to transform XYZ to $X'Y'Z'$ (figure A.1). The presentation for a vector in $X'Y'Z'$ and XYZ can be linked by a matrix, $A_R(\psi_x, \psi_y, \psi_z)$:

$$A_R(\psi_x, \psi_y, \psi_z) = A_z(\psi_z)A_y(\psi_y)A_x(\psi_x) =$$
$$\begin{pmatrix} cos\psi_y cos\psi_z & sin\psi_x sin\psi_y cos\psi_z - cos\psi_x sin\psi_z & cos\psi_x sin\psi_y cos\psi_z + sin\psi_x sin\psi_z \\ cos\psi_y sin\psi_z & sin\psi_x sin\psi_y sin\psi_z + cos\psi_x cos\psi_z & cos\psi_x sin\psi_y sin\psi_z - sin\psi_x cos\psi_z \\ -sin\psi_y & sin\psi_x cos\psi_y & cos\,\psi_x cos\psi_y \end{pmatrix} \tag{A1.4}$$

We call $A_R(\psi_x, \psi_y, \psi_z)$ as the coordinates rotation matrix.

https://doi.org/10.5194/amt-2020-353
Preprint. Discussion started: 14 September 2020

A.2 AoA measuring errors

In coordinate XYZ, AoA includes zenith angle θ and azimuth angle ϕ. The AoA is determined by two phase differences $\Delta\Psi_1$ and $\Delta\Psi_2$. $\Delta\Psi_1$ and $\Delta\Psi_2$ are caused by the antenna array length D_1 and D_2 in the Jones configuration. Taking one antenna array as an example, the radio wave is at angle γ with an antenna array (figure A.2), and there is a phase difference between the two ends of the antenna array. Hence, $\Delta\Psi_1$ and $\Delta\Psi_2$ can be expressed as:

$$\Delta\Psi_1 = \frac{2\pi D_1 cos\gamma_1}{\lambda} \quad \text{(A2.1)}$$

$$\Delta\Psi_2 = \frac{2\pi D_2 cos\gamma_2}{\lambda} \quad \text{(A2.2)}$$

The relationship between θ, ϕ and γ_1, γ_2 can be expressed as:

$$\cos^2\gamma_1 + \cos^2\gamma_2 + \cos^2\theta = 1 \quad \text{(A2.3)}$$

$$tan\phi = \frac{cos\gamma_2}{cos\gamma_1} \quad \text{(A2.4)}$$

Or in another kind of expression:

$$\cos\gamma_1 = \sin\theta\cos\phi \quad \text{(A2.5)}$$

$$\cos\gamma_2 = \sin\theta\sin\phi \quad \text{(A2.6)}$$

substitute $cos\gamma_1$ and $cos\gamma_2$ in (A2.3) and (A2.4) using (A2.1) and (A2.2):

$$\cos^2\theta = 1 - \left(\frac{\lambda}{2\pi}\right)^2 \left(\frac{\Delta^2\Psi_1}{D_1^2} + \frac{\Delta^2\Psi_2}{D_2^2}\right) \quad \text{(A2.7)}$$

$$\ln(\tan\phi) = \ln(D_2\Delta\Psi_2) - \ln(D_1\Delta\Psi_1) \quad \text{(A2.8)}$$

(A2.7) and (A2.8) are the equations that link the phase difference with the AoA. Use Taylor expansion of θ, ϕ, $\Delta\Psi_1$ and $\Delta\Psi_2$ to first order for (A2.7) and (A2.8), then subtract (A2.7) and (A2.8).

$$2cos\theta sin\theta\delta\theta = \left(\frac{\lambda}{2\pi}\right)^2 \left[\frac{2\Delta\Psi_1\delta(\Delta\Psi_1)}{D_1^2} + \frac{2\Delta\Psi_2\delta(\Delta\Psi_2)}{D_2^2}\right] \quad \text{(A2.9)}$$

$$\delta\phi = \frac{sin\phi cos\phi}{\Delta\Psi_2}\delta(\Delta\Psi_2) - \frac{sin\phi cos\phi}{\Delta\Psi_1}\delta(\Delta\Psi_1) \quad \text{(A2.10)}$$

Finally, substitute $\Delta\Psi_1$ and $\Delta\Psi_2$ to form θ, ϕ using (A2.1), (A2.2) and (A2.5), (A2.6). Now, eq. (3) and eq. (4) have been proven. If the zenith angle $\theta = 0°$, we stipulate that $\frac{\cos\phi}{\sin\theta}$ and $\frac{\sin\phi}{\sin\theta}$ are 1.

A.3 Radial distance measuring error

Use the Taylor expansions of R_t, R and $cos\alpha$ to first order for eq. (1) and then subtract eq. (1) to obtain $\delta\mathrm{R_t}$ as a function of $\delta\mathrm{R}$ and $\delta(\cos\alpha)$:

$$\delta\mathrm{R_t} = \frac{\mathrm{R^2-2Rd\cos\alpha+d^2}}{2(\mathrm{R-d\cos\alpha})^2}\delta\mathrm{R} + \frac{\mathrm{d(R^2-d^2)}}{2(\mathrm{R-d\cos\alpha})^2}\delta(\cos\alpha) \tag{A3.1}$$

α is the angle between R_t and axis-X_i'. In coordinate-$X_i'Y_i'Z_i'$, we denote the zenith and azimuth angles as θ' and ϕ', respectively. The relationship between α and θ', ϕ' is

$$cos\alpha = \ sin\theta' \ cos\phi' \tag{A3.2}$$

Using coordinates rotation matrix $A_R(\psi_x^{\mathrm{X,i}}, \psi_y^{Y,\mathrm{i}}, \psi_z^{Z,\mathrm{i}})$ and denoting the 3x3 matrix A_R's elements as A_{ij}, we can express $sin\theta' cos\phi'$ as the function of AoA:

$$\sin\theta'\cos\phi' = \mathrm{A_{11}}\sin\theta\cos\phi + \mathrm{A_{12}}\sin\theta\sin\phi + \mathrm{A_{13}}\cos\theta \tag{A3.3}$$

Using (A3.2) and (A3.3), we can express $\delta(\cos\alpha)$ as a function of $\delta\theta$ and $\delta\phi$.

$$\delta(\cos\alpha) = (\mathrm{A_{11}}\cos\theta\cos\phi + \mathrm{A_{12}}\cos\theta\sin\phi - \mathrm{A_{13}}\sin\theta)\delta\theta + (-\mathrm{A_{11}}\sin\theta\sin\phi + \mathrm{A_{12}}\sin\theta\cos\phi)\delta\phi \tag{A3.4}$$

Finally, we can express $\delta\mathrm{R_t}$ as the function of $\delta R, \delta\theta, \delta\phi$.

$$\delta R_t = F(\delta R, \delta\theta, \delta\phi) = f_R(\theta,\phi)\delta R + f_\theta(\theta,\phi)\delta\theta + f_\phi(\theta,\phi)\delta\phi \tag{A3.5}$$

for

$$f_R(\theta,\phi) = \frac{d^2+R^2-2Rd(\mathrm{A_{11}}\sin\theta cos\phi+A_{12}sin\theta sin\phi+A_{13}cos\theta)}{2[R-d(\mathrm{A_{11}}\sin\theta cos\phi+A_{12}sin\theta sin\phi+A_{13}cos\theta)]^2}$$

(A3.6)

$$f_\theta(\theta,\phi) = \frac{d(R^2-d^2)(\boldsymbol{A_{11}cos\theta cos\phi+A_{12}cos\theta sin\phi-A_{13}sin\theta})}{2[R-d(\mathrm{A_{11}}\sin\theta cos\phi+A_{12}sin\theta sin\phi+A_{13}cos\theta)]^2}$$

(A3.7)

$$f_\phi(\theta,\phi) = \frac{d(R^2-d^2)(\boldsymbol{-A_{11}sin\theta sin\phi+A_{12}sin\theta cos\phi})}{2[R-d(\mathrm{A_{11}}\sin\theta cos\phi+A_{12}sin\theta sin\phi+A_{13}cos\theta)]^2} \tag{A3.8}$$

A.4 True error of E_2

See figure 4 (b), side AC adding side CB represents the pulse width. Side AC equals side CB, which equals half the pulse width, S. In $\boldsymbol{X_i'Y_i'Z_i'}$, the presentation of point A is $(\mathrm{x_0, y_0, z_0})$, the receiver is (0,0,0) and T_i is (d,0,0). The distance between T_i and A is $R_1 = R - R_t$. We denote that the coordinate of B is (x_B, y_B, z_B) and C is (x_C, y_C, z_C). We use vector collinear to establish equations for B and C. Therefore, we can obtain the coordinates of B and C by the following equations:

https://doi.org/10.5194/amt-2020-353
Preprint. Discussion started: 14 September 2020

$$(x_B, y_B, z_B)^T = \frac{R_t - S}{R_t}\ (x_0, y_0, z_0)^T \tag{A4.1}$$

$$(x_C - d, y_C, z_C)^T = \frac{R_1 - S}{R_1}\ (x_0 - d, y_0, z_0)^T \tag{A4.2}$$

For isosceles triangle ABC, the perpendicular line AD intersects side CB in middle point D. Then, we obtain the coordinate of D in $X_i'Y_i'Z_i'$:

$$(\mathrm{x_D}, \mathrm{y_D}, \mathrm{z_D}) = \frac{1}{2}(\mathrm{x_B} + \mathrm{x_c}, \mathrm{y_B} + \mathrm{y_c}, \mathrm{z_b} + \mathrm{z_c}) = \frac{1}{2}((\mathrm{a_1} + \mathrm{a_2})\mathrm{x_0} - \mathrm{a_2 d} + \mathrm{d}, (\mathrm{a_1} + \mathrm{a_2})\mathrm{y_0}, (\mathrm{a_1} + \mathrm{a_2})\mathrm{z_0}) \tag{A4.3}$$

We denote $a_1 = \frac{R_t - S}{R_t}$. $a_2 = \frac{R_1 - S}{R_1}$. Finally, we can obtain the true error of $\mathrm{E_2}$ as vector $\overrightarrow{DA}$ in $X_i'Y_i'Z_i'$:

$$\boldsymbol{\overrightarrow{DA}} = \left(\frac{(2 - a_1 - a_2)x_0 + d(a_1 - 1)}{2}, \frac{2 - a_1 - a_2}{2}\boldsymbol{y_0}, \frac{2 - a_1 - a_2}{2}\boldsymbol{z_0}\right)^{\boldsymbol{T}} \tag{A4.4}$$

A.5 error propagation of $\boldsymbol{E_1}$

From $XYZ\ \ to\ \ X_0'Y_0'Z_0'$, we need coordinates rotation matrix $A_R^{(XYZ, X_0'Y_0'Z_0')}$

$$A_R^{(XYZ, X_0'Y_0'Z_0')} = A_R(\Psi_x^{i,0}, \Psi_y^{i,0}, \Psi_z^{i,0}) \cdot A_R(\psi_x^{\mathrm{X,i}}, \psi_y^{Y,\mathrm{i}}, \psi_z^{Z,\mathrm{i}}) \tag{A5.1}$$

We denote 3×3 matrix $A_R^{(XYZ, X_0'Y_0'Z_0')}$ as A_{ij}^0 and $A_R(\Psi_x^{i,0}, \Psi_y^{i,0}, \Psi_z^{i,0})$ as A_{ij}'. Thus, $A_{ij}^0 = A_{ik}'A_{kj}$. The true error of $\mathrm{E_1}$ can be expressed as a vector in XYZ, which can be decomposed into three orthogonal error vectors, as shown in eq. (6)-(8). Using $A_R^{(XYZ, X_0'Y_0'Z_0')}$, we can transform those three vectors in the presentation of $X_0'Y_0'Z_0'$ as:

$$\overrightarrow{\delta \mathrm{R_t}'} = \mathrm{A_R^{(XYZ, X_0'Y_0'Z_0')}} \cdot \overrightarrow{\delta \mathrm{R_t}}$$

$$= \delta\mathrm{R_t} \cdot \mathrm{A_R^{(XYZ, X_0'Y_0'Z_0')}} \cdot (\sin\theta\cos\phi, \sin\theta\sin\phi, \cos\theta)^{\mathrm{T}}$$

$$= \left(\mathrm{f_R}(\theta,\phi)\delta\mathrm{R} + \mathrm{f_\theta}(\theta,\phi)\delta\theta + \mathrm{f_\phi}(\theta,\phi)\delta\phi\right) \cdot \left(\mathrm{X_0'}(\delta\mathrm{R_t}), \mathrm{Y_0'}(\delta\mathrm{R_t}), \mathrm{Z_0'}(\delta\mathrm{R_t})\right)^{\mathrm{T}}$$

$$\overrightarrow{\mathrm{R_t}\delta\theta\,'} = A_R^{(XYZ, X_0'Y_0'Z_0')} \cdot \overrightarrow{R_t\delta\theta}$$

$$= R_t\delta\theta \cdot A_R^{(XYZ, X_0'Y_0'Z_0')} \cdot (-cos\theta cos\phi, -cos\theta sin\phi, sin\theta)^T$$

$$= R_t\delta\theta \cdot (X_0'(\delta\theta), Y_0'(\delta\theta), Z_0'(\delta\theta))^T$$

$$\overrightarrow{\mathrm{R_t}\sin\theta\delta\phi\,'} = A_R^{(XYZ, X_0'Y_0'Z_0')} \cdot \overrightarrow{R_t sin\theta\delta\phi}$$

$$= R_t sin\theta\delta\phi \cdot A_R^{(XYZ, X_0'Y_0'Z_0')} \cdot (-sin\phi, cos\phi, 0)^T$$

https://doi.org/10.5194/amt-2020-353
Preprint. Discussion started: 14 September 2020

$$= \quad R_t sin\theta\delta\phi \cdot (X_0'(\delta\phi), Y_0'(\delta\phi), Z_0'(\delta\phi))^T \tag{A5.2}$$

For

$$\begin{pmatrix} X_0'(\delta R_t) & X_0'(\delta\theta) & X_0'(\delta\phi) \\ Y_0'(\delta R_t) & Y_0'(\delta\theta) & Y_0'(\delta\phi) \\ Z_0'(\delta R_t) & Z_0'(\delta\theta) & Z_0'(\delta\phi) \end{pmatrix} = A^{(XYZ, X_0'Y_0'Z_0')} \begin{pmatrix} sin\theta cos\phi & -cos\theta cos\phi & -sin\phi \\ sin\theta sin\phi & -cos\theta sin\phi & cos\phi \\ cos\theta & sin\theta & 0 \end{pmatrix} \tag{A5.3}$$

Therefore, in $X_0'Y_0'Z_0'$, the true error of E_1 can be expressed as vector $\left(\delta_{(1)}X_0', \delta_{(1)}Y_0', \delta_{(1)}{Z'}_0\right)^T$:

$$\delta_{(1)}X_0' \quad = \quad f_R(\theta,\phi)X_0'(\delta R_t)\delta R + \left(f_\theta(\theta,\phi)X_0'(\delta R_t) + R_t X_0'(\delta\theta)\right)\delta\theta + (f_\phi(\theta,\phi)X_0'(\delta R_t) + \ R_t sin\theta X_0'(\delta\phi))\delta\phi$$

$$\delta_{(1)}Y_0' \quad = \quad f_R(\theta,\phi)Y_0'(\delta R_t)\delta R + \left(f_\theta(\theta,\phi)Y_0'(\delta R_t) + R_t Y_0'(\delta\theta)\right)\delta\theta + (f_\phi(\theta,\phi)Y_0'(\delta R_t) + \ R_t sin\theta Y_0'(\delta\phi))\ \delta\phi$$

$$\delta_{(1)}Z_0' \quad = \quad f_R(\theta,\phi)Z_0'(\delta R_t)\delta R + \left(f_\theta(\theta,\phi)Z_0'(\delta R_t) + R_t Z_0'(\delta\theta)\right)\delta\theta + (f_\phi(\theta,\phi)Z_0'(\delta R_t) + \ R_t sin\theta Z_0'(\delta\phi))\ \delta\phi \tag{A5.4}$$

For simplicity, we can write (A.26) in the form of a matrix:

$$\begin{pmatrix} \delta X_0' \\ \delta Y_0' \\ \delta {Z'}_0 \end{pmatrix} = \begin{pmatrix} X_0'(\delta R_t) & X_0'(\delta\theta) & X_0'(\delta\phi) \\ Y_0'(\delta R_t) & Y_0'(\delta\theta) & Y_0'(\delta\phi) \\ Z_0'(\delta R_t) & Z_0'(\delta\theta) & Z_0'(\delta\phi) \end{pmatrix} \cdot \begin{pmatrix} f_R(\theta,\phi) & f_\theta(\theta,\phi) & f_\phi(\theta,\phi) \\ 0 & R_t & 0 \\ 0 & 0 & R_t sin\theta \end{pmatrix} \begin{pmatrix} \delta R \\ \delta\theta \\ \delta\phi \end{pmatrix} \tag{A5.5}$$

https://doi.org/10.5194/amt-2020-353
Preprint. Discussion started: 14 September 2020

Atmospheric Measurement Techniques
Open Access
EGU
Discussions

Table 1: parameters settings of pictures in the paper

Table 1. Parameter settings

	Figure 7	Figure 8(a)	Figure 8(b)	Figure 8(c)
d /km	300	0	150	150
$(\psi_x^{X,i}, \psi_y^{Y,i}\ \psi_z^{Z,i})$	$(0, 0, -45°)$	$(0, 0, 0)$	$(0, 0, -45°)$	$(5, 5\ -45°)$
$(\psi_x^{i,0}, \psi_y^{i,0}\ \psi_z^{i,0})$	$(0, 0, 45°)$	$(0, 0, 0)$	$(0, 0, 45°)$	$(0, 0, 45°)$
$(\delta R\ , \delta(\Delta\Psi_1)\ , \delta(\Delta\Psi_2))$	$(6.3, 35°, -45°)$	$(6.3, 35°, -45°)$	$(6.3, 35°, -45°)$	$(6.3, 35°, -45°)$
$(\frac{D_1}{\lambda}, \frac{D_2}{\lambda})$	$(4.5\ , 4.5)$	$(4.5\ , 4.5)$	$(4.5\ , 4.5)$	$(4.5\ , 4.5)$
S /km	2	2	2	2
PRFs/HZ	625	625	625	625

Unit: δR /km

https://doi.org/10.5194/amt-2020-353
Preprint. Discussion started: 14 September 2020

Atmospheric Measurement Techniques Discussions

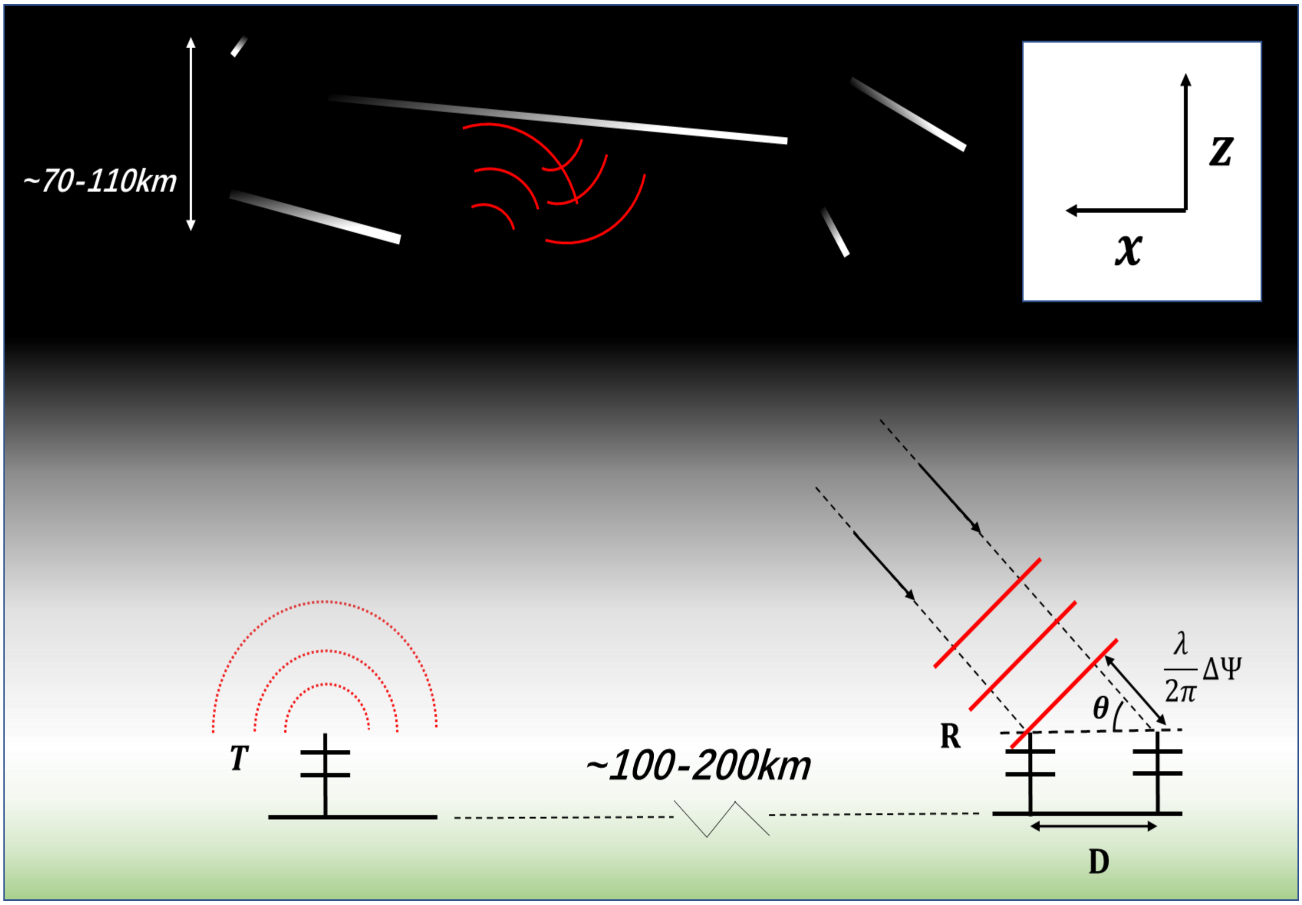

Figure 1: Schematic diagram of the bistatic configuration in the HM. The two receiver antennas and the transmitter antenna are collinear. The analysis is in a 2-dimensional vertical plane through the baseline.

https://doi.org/10.5194/amt-2020-353
Preprint. Discussion started: 14 September 2020

Atmospheric Measurement Techniques Discussions

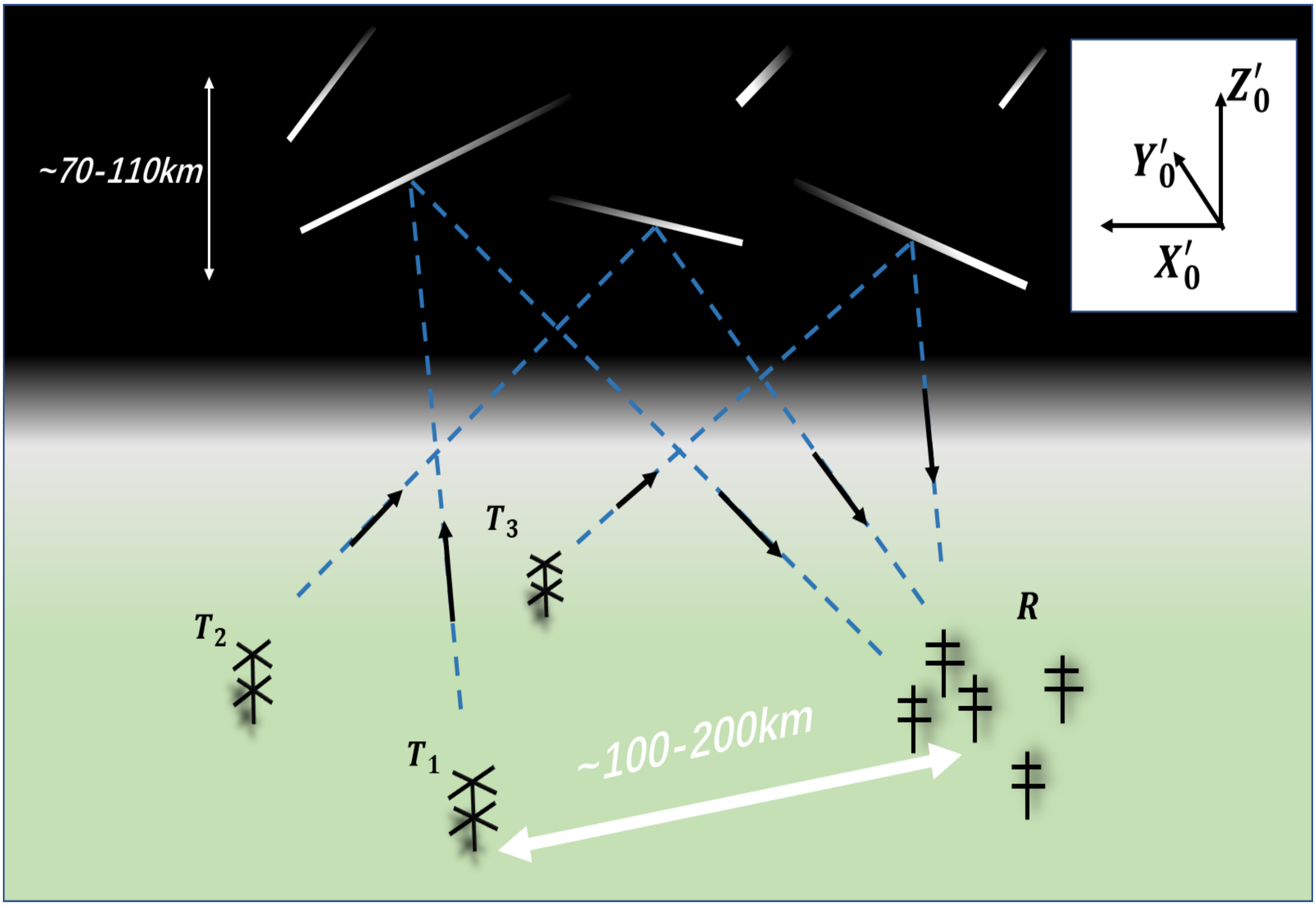

Figure 2: Schematic diagram of the multistatic meteor radar system. There are three transmitters (T_1, T_2 and T_3) and one receiver (R) in the picture. The distance between the transmitter and receiver is usually approximately 100-200 km. $X_0^{'}, Y_0^{'}, Z_0^{'}$ represents the west, north and up directions in the receiver.

https://doi.org/10.5194/amt-2020-353
Preprint. Discussion started: 14 September 2020

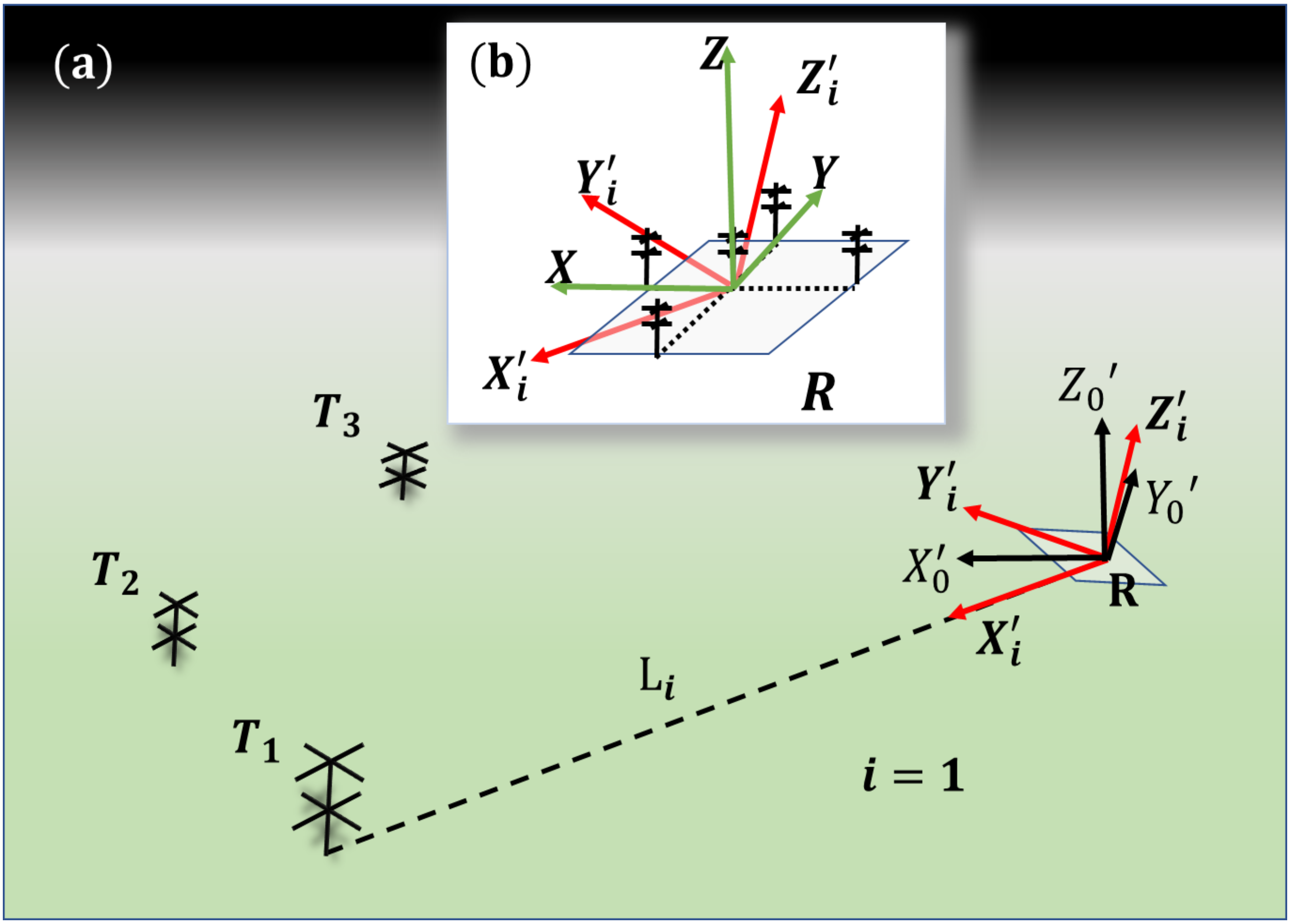

Figure 3: (a) Schematic diagram of three coordinate systems. $X_i^{'}Y_i^{'}Z_i^{'}$ are a class of coordinate systems. In this picture, i can be 1,2,3. (b) Magnified plot of the receiver. XYZ is fixed on the receiver horizontal plane. Axis-X and Y are collinear to two antenna arrays.

https://doi.org/10.5194/amt-2020-353
Preprint. Discussion started: 14 September 2020

Atmospheric Measurement Techniques
Discussions

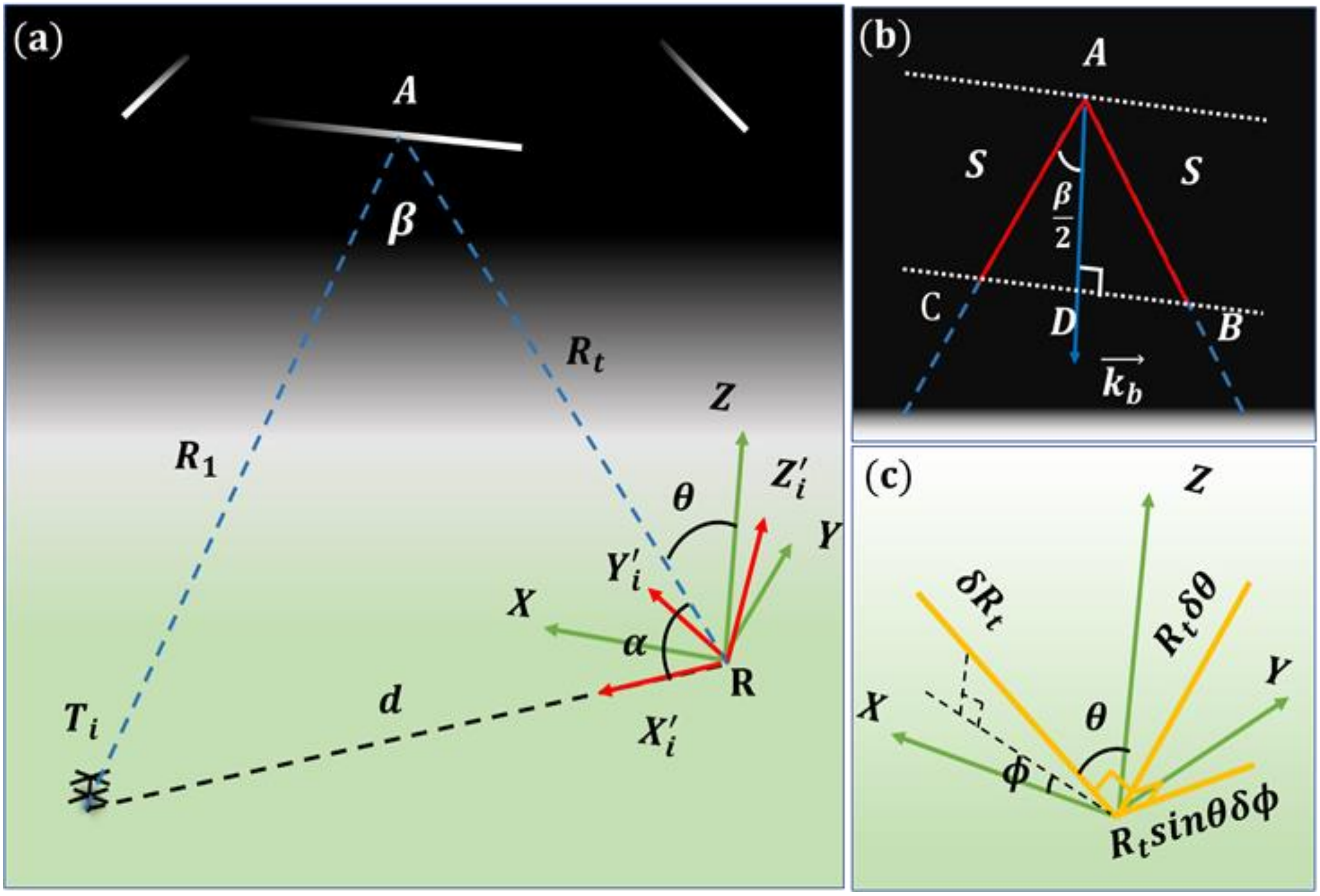

Figure 4: (a) Schematic diagram of a forward scatter geometry for the radar link between T_i and R. A is the meteor trail reflection point. (b) Magnified plot of reflection point A. The red line represents one radio wave pulse, and S is the half pulse length. $\overrightarrow{k_b}$ is the Bragg vector and halves forward scatter angle β. (c) Schematic diagram of E_1 in XYZ, which can be decomposed into three orthogonal vectors.

https://doi.org/10.5194/amt-2020-353
Preprint. Discussion started: 14 September 2020

Atmospheric Measurement Techniques
Discussions

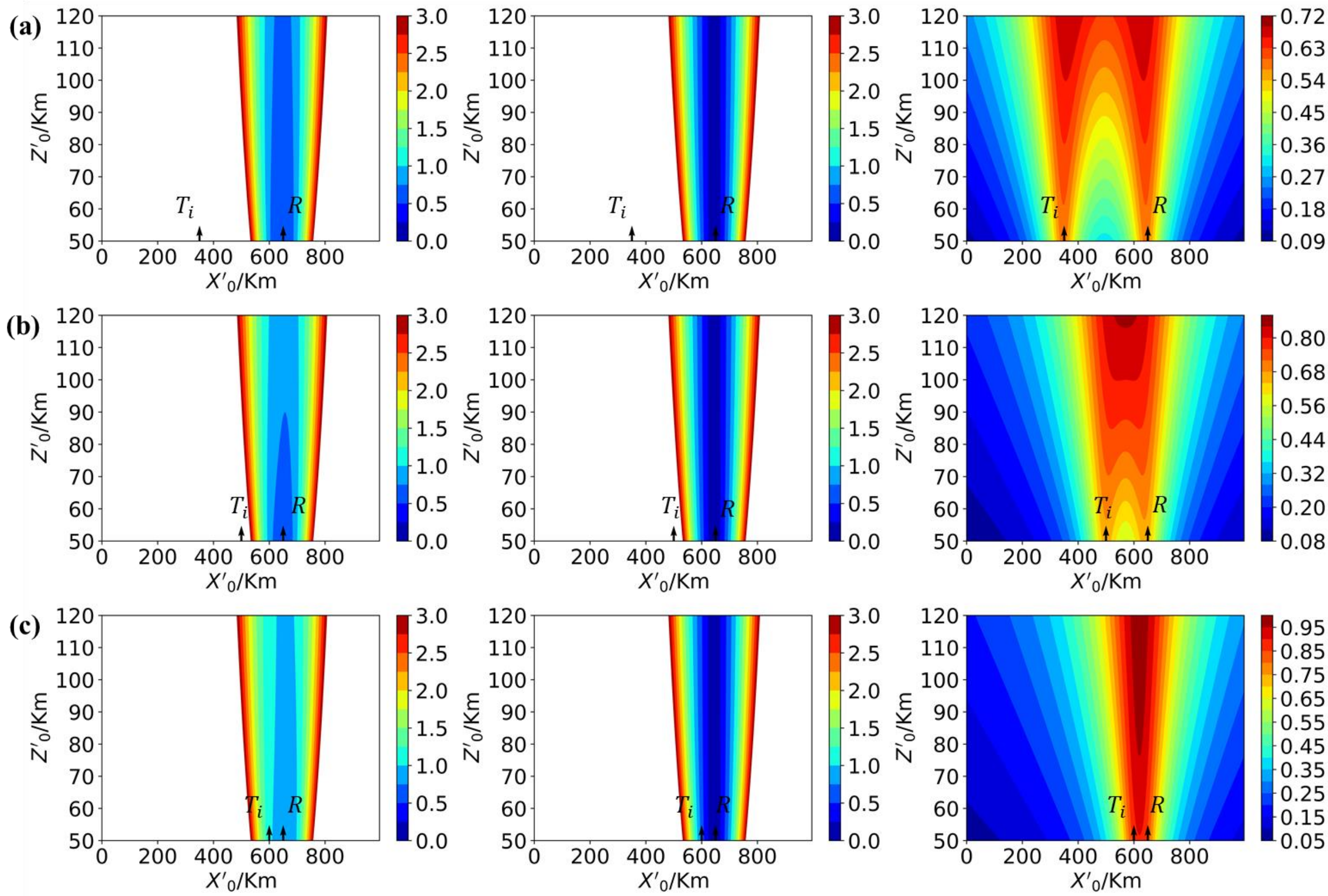

Figure 5: Two-dimensional space normalized vertical spatial resolution distribution ignoring the error term "δR_t" (corresponding to the HM). In (a) and (b), d equals 300, 150, and 50 km. For each row from left to right, they are "total vertical resolution distribution", "vertical resolution distribution related to error term $\overrightarrow{R_t\delta\theta}$" and "vertical resolution distribution related to E_2". Only the normalized vertical spatial resolutions less than 3 km are shown. The normalized spatial resolution is one quarter of the spatial resolution. Details are provided in the text.

https://doi.org/10.5194/amt-2020-353
Preprint. Discussion started: 14 September 2020

Atmospheric Measurement Techniques
Discussions

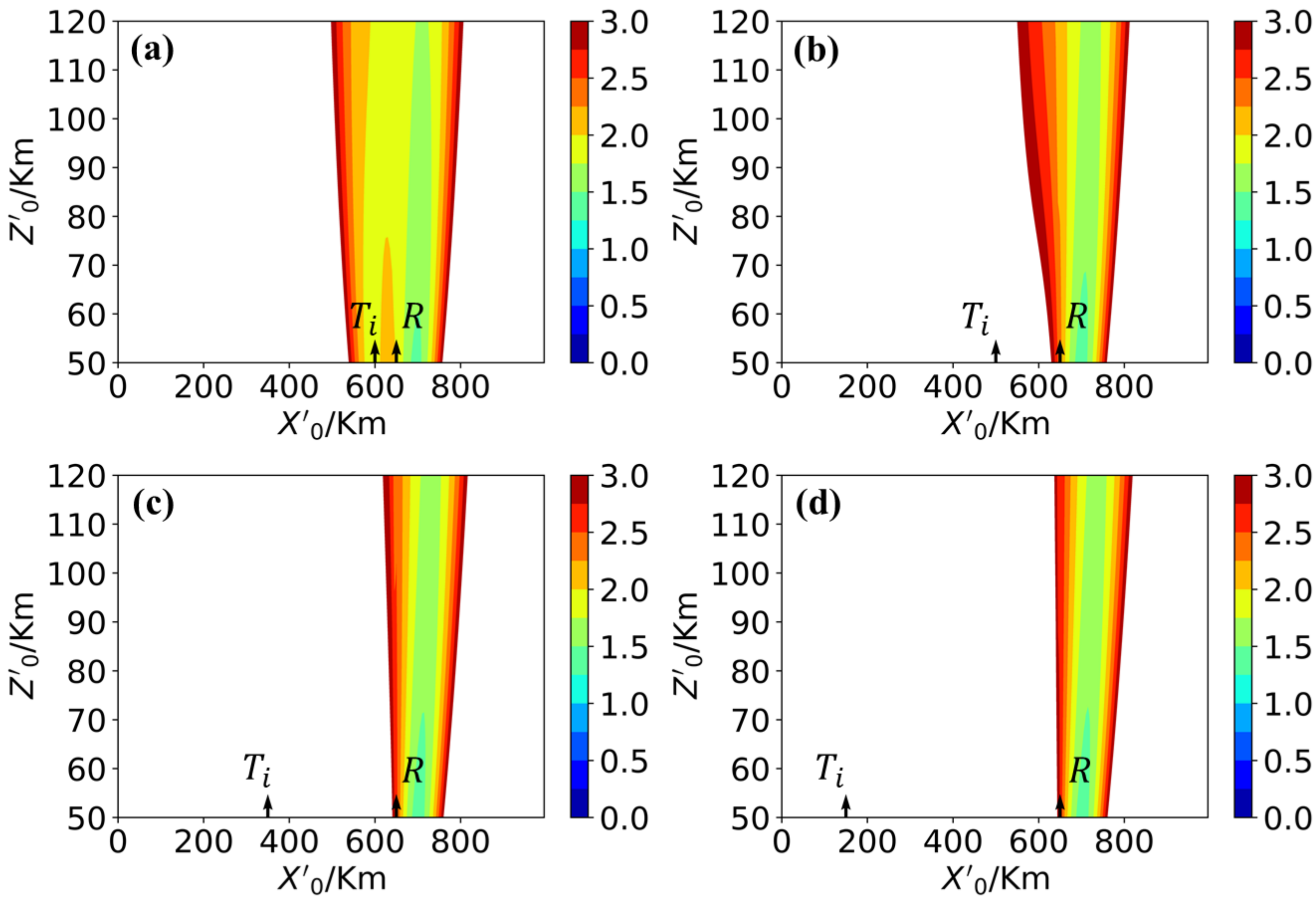

Figure 6: Normalized vertical spatial resolution distribution in the two-dimensional vertical plane considering the error term "$\overrightarrow{\delta R_t}$". In (a) and (b), d is 50, 150, 300, 500 km. Only the normalized vertical spatial resolutions less than 3 km (corresponding to a 12 km vertical spatial resolution) are shown.

https://doi.org/10.5194/amt-2020-353
Preprint. Discussion started: 14 September 2020

Atmospheric Measurement Techniques
Discussions

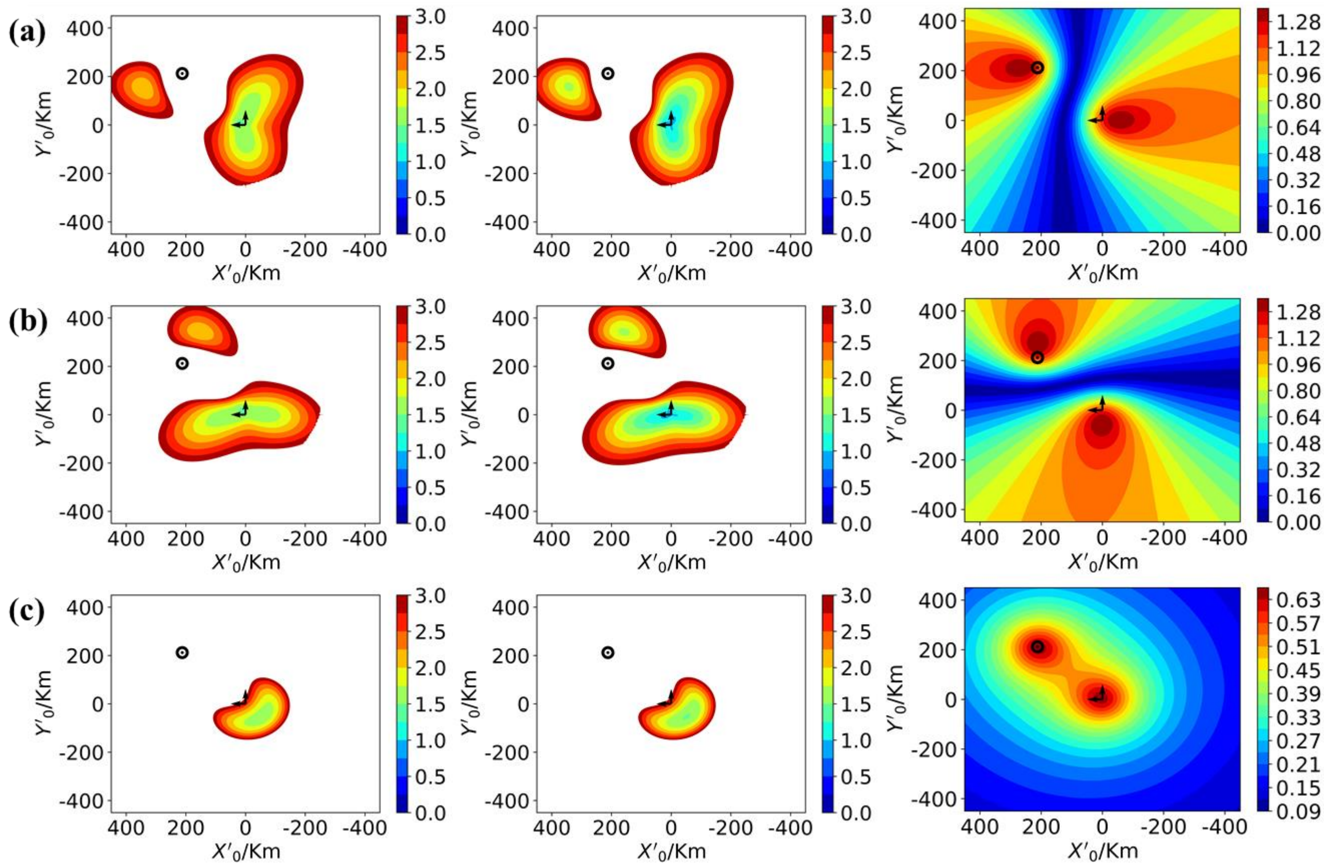

Figure 7: Normalized three-dimensional spatial resolution distributions in three-dimensional space. From (a) to (c) is the normalized spatial resolution in the X_0', Y_0', Z_0' direction. For each row from left to right, they are "total resolution", "E_1 related", and "E_2 related" distributions. The black dot represents transmitter T_i, and the black right-angle arrow represents receiver R. d is 300 km; details are provided in the text.

https://doi.org/10.5194/amt-2020-353
Preprint. Discussion started: 14 September 2020

Atmospheric Measurement Techniques
Discussions

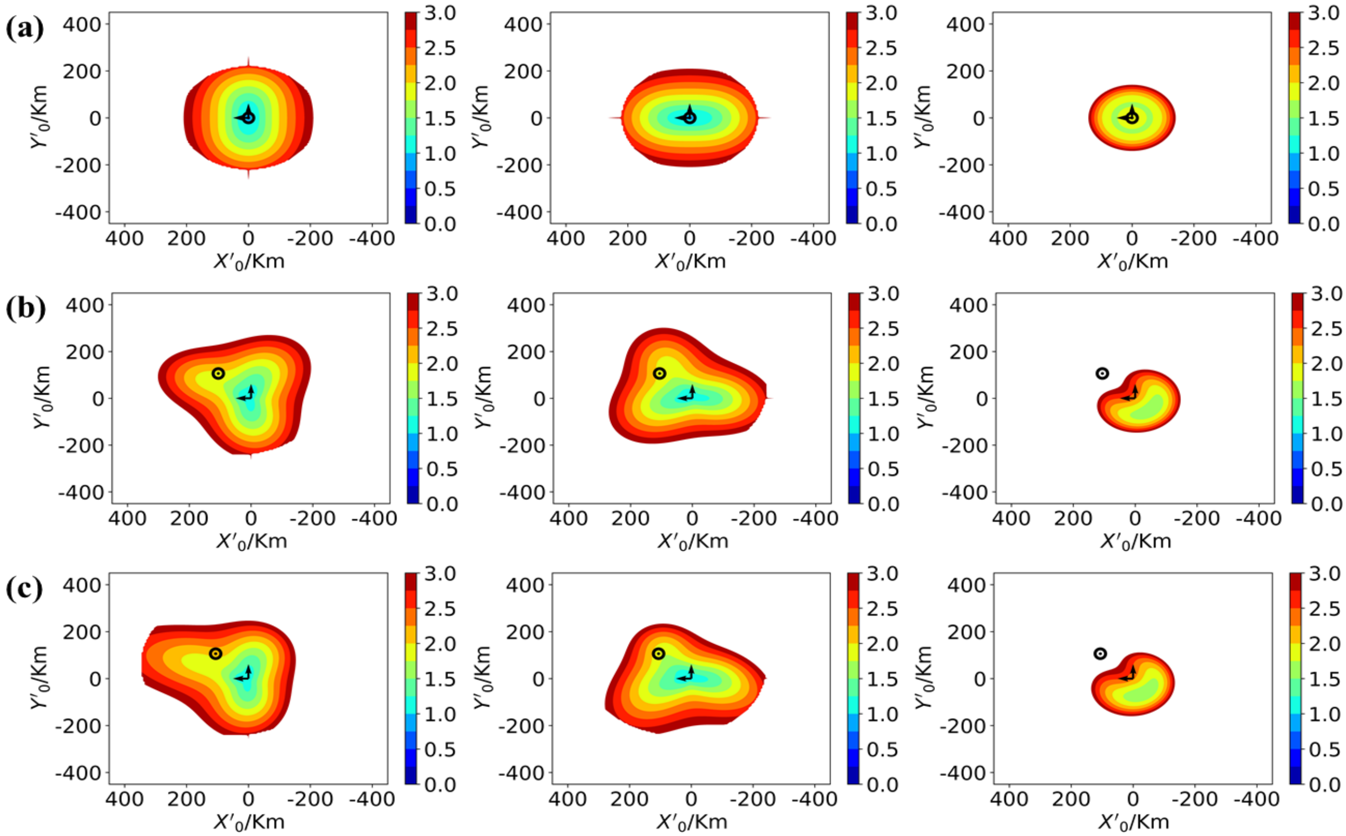

Figure 8: Normalized three-dimensional spatial resolution distributions in three-dimensional space with three different settings. (a) $d = 0$, monostatic meteor radar (b) $d = 150km$, $\psi_x^{X,i} = \psi_y^{Y,i} = 0$ (c) $d = 150km$, $\psi_x^{X,i} = \psi_y^{Y,i} = 5°$. Each row from left to right are the resolution distributions in the X_0', Y_0', Z_0' direction, respectively.

https://doi.org/10.5194/amt-2020-353
Preprint. Discussion started: 14 September 2020

Atmospheric Measurement Techniques Discussions
Open Access

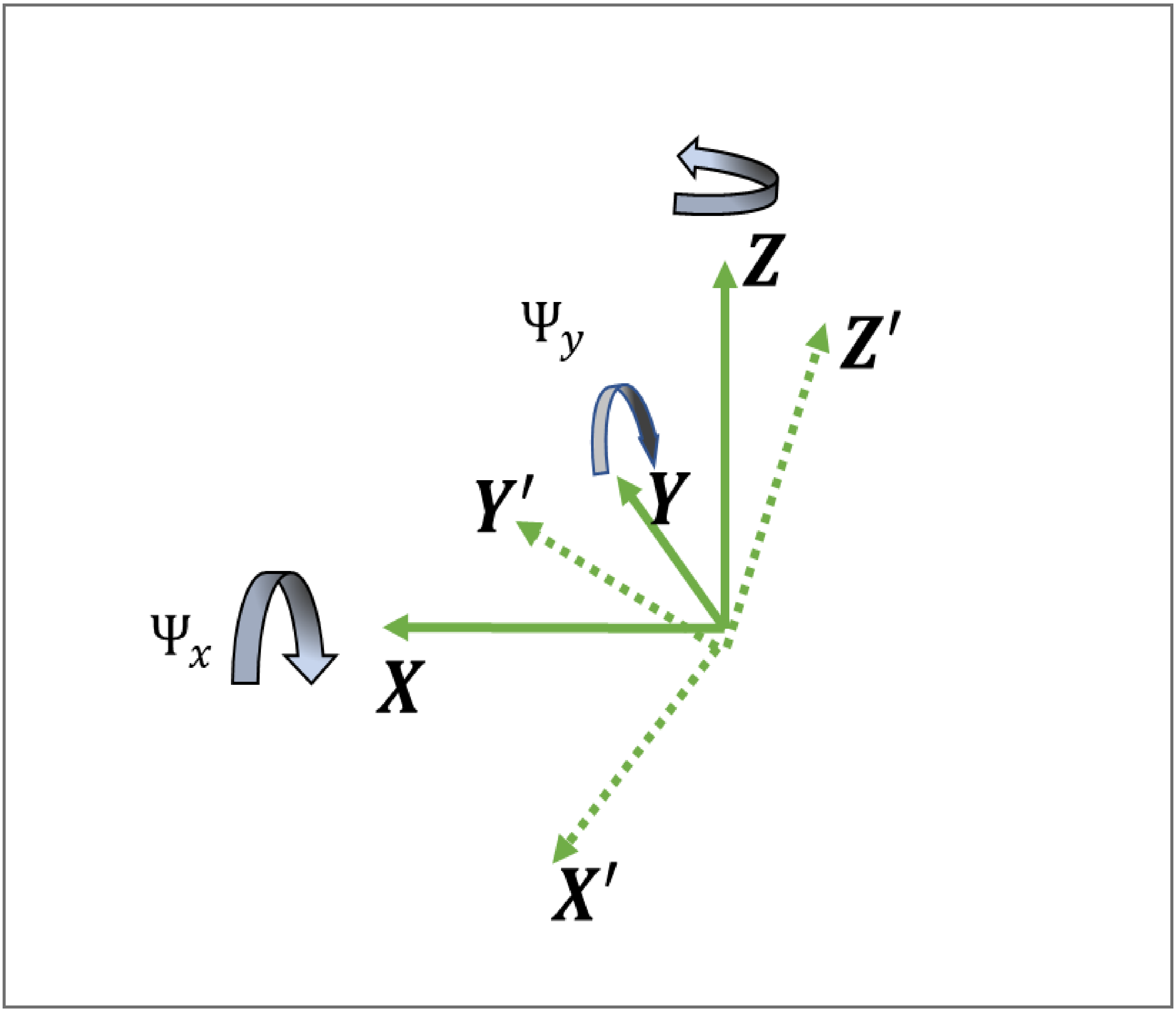

Figure A.1

https://doi.org/10.5194/amt-2020-353
Preprint. Discussion started: 14 September 2020

Atmospheric Measurement Techniques
Discussions

590

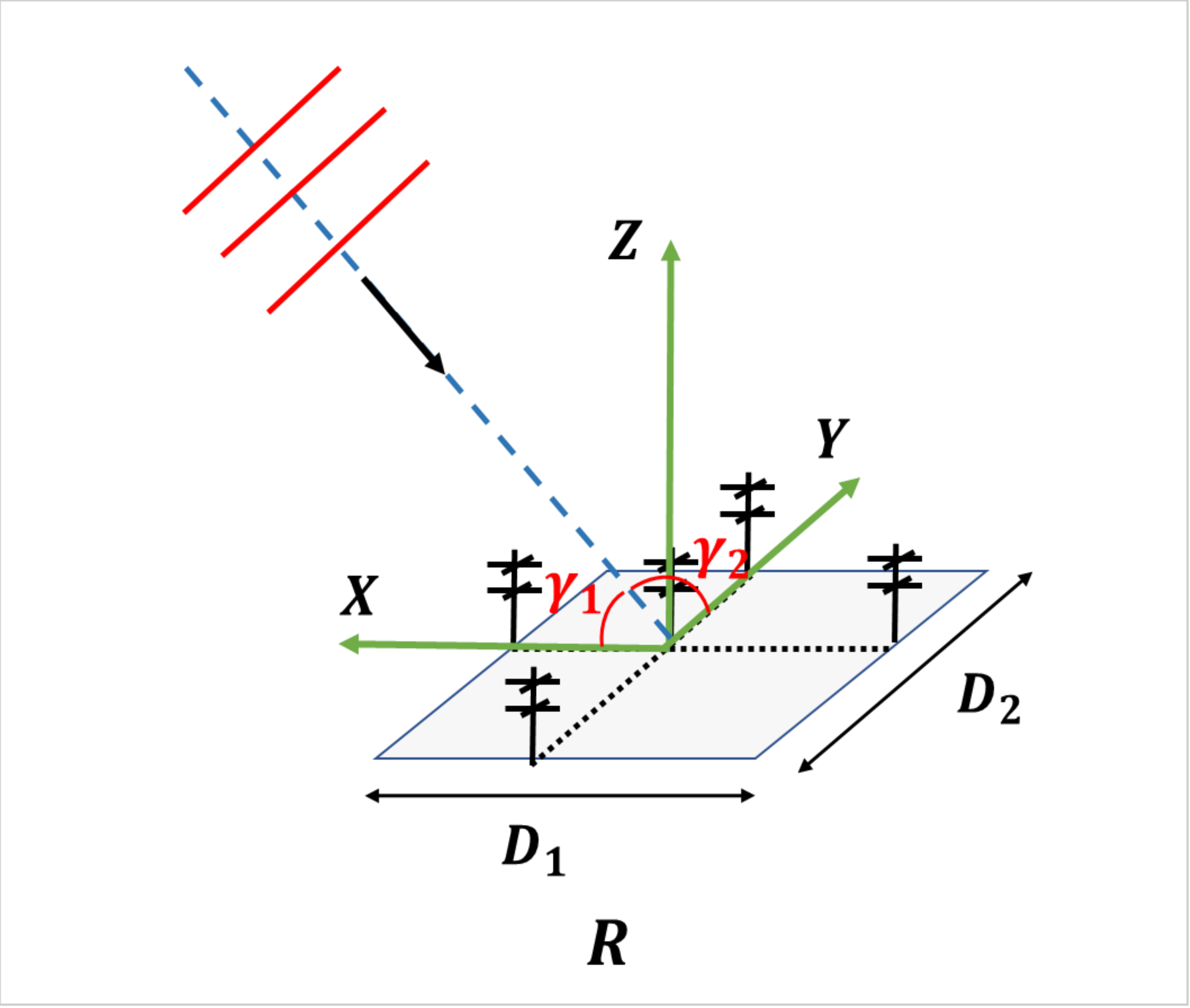

Figure A.2